Experimental investigation of the vortical activity in the close wake of a simplified military transport aircraft

Yannick Bury · Thierry Jardin · Andreas Klöckner

Abstract This paper focuses on the experimental characterization of the vortex structures that develop in the aft fuselage region and in the wake of a simplified geometry of a military transport aircraft. It comes within the framework of the military applications of airflow influence on airdrop operations. This work relies on Particle Image Velocimetry (PIV) measurements combined with a vortex-tracking approach. Complex vortex dynamics is revealed, in terms of vortex positions, intensities, sizes, shapes and fluctuation levels, for both closed and opened cargo-door and ramp airdrop configurations.

1 Introduction

Military transport aircrafts differ from other aircrafts by the shape of their aft fuselage portion. In order to perform operational missions, such as deployment of airborne troops or delivery of cargo/supplies to frontline troops or humanitarian disaster areas, it is necessary to drop cargo or troops from a large cargo-bay ramp located at the rear of the aircraft. Consequently, this aft fuselage portion is asymmetrically designed, with a pronounced upsweep of its lower contour. This region is referred to as the upsweep region. The upsweep angle, defined as the angle between the mean upsweep line and the fuselage axis, can reach values up to 28°, as for the Lockheed C-130 Hercules. Because of this rapidly decreasing fuselage cross-sectional area, strong adverse longitudinal pressure gradients occur in the upsweep region, leading to massive separation of the flow. A first resulting drawback is an increase of the fuselage form drag [1]. The highly three-dimensional flow separation area is also characterized by the presence of a pair of large counter-rotating

Y. Bury (✉) · T. Jardin · A. Klöckner
Université de Toulouse, ISAE, Toulouse, 31055, France
E-mail: yannick.bury@isae.fr
Tel.: +33-561339198
Fax: +33-561339163

vortices, the upsweep vortices [2–5]. The corresponding vorticity vectors are grossly aligned with the freestream velocity. As a consequence, a consistent upward flow is observed throughout the central region, aft of the cargo-bay and close to the aircraft plane of symmetry. The resulting flow field pattern persists in the wake of the aircraft as the vortices are advected downstream. In airdrop operations, the upsweep vortices can induce problems when objects are caught within this region. In particular, this can result in the followings: objects touching the empennage on exit from the rear door; initial trajectories of airdropped payloads or paratroopers perturbed; extraction-phase delay due to partial efficiency loss of extraction parachute; or the opening of the decelerating parachute delayed [6].

The vortex dynamics in the aft fuselage portion and in the close wake of the aircraft can thus be supposed to decompose into the following sequences: separation and rolling-up of the fuselage boundary layer into the upsweep vortex under the influence of a strong adverse pressure gradient, interaction of the vortex with the upsweep wall and with the empennage, probable inception of a counter-rotating vortex resulting from the interaction of the upsweep vortex with the empennage, vortex-vortex interaction in the wake of the aircraft. Moreover this scenario is being played out in the presence of a consistent streamwise and upward flow and of a strong adverse longitudinal pressure gradient.

Previous studies have investigated the interaction of a primary vortex or a pair of counter-rotating vortices with a wall and with a wall-bounded shear layer [7–10], revealing 1) its strong influence on the production of turbulence kinetic energy and on the shear stress levels experienced in both the boundary layer and the vortex cores, 2) the occurrence of short wavelength elliptic instabilities in the secondary vortices, that tend to affect the primary vortex when the Reynolds number is increased. However these studies are essentially conducted in quiescent fluid or in the presence of a weak head- or cross-wind.

The dynamics of counter-rotating vortices in free field has been much more widely studied, either numerically, experimentally or theoretically [11–14]. These studies emphasize a complex, multi-stage evolution of various short to long wavelength instabilities. The variety of potential instabilities is shown to largely depend, amongst others, on both axial-core flow and vortex separation distance. They have also identified that the background turbulence, inherent to fluid motion, was responsible for the transient growth of a vortex displacement mode, resulting in the meandering of the vortices. One should however notice that most of these studies exclusively considered vortices evolving in a quiescent fluid.

Lastly, although the variety of technical applications where it is, voluntarily or not, involved and despite numerous researches since the early 60's [15–18], the vortex breakdown phenomenon still suffers a lack of comprehension. Ruith and co-authors [19], in their study about the three-dimensional vortex breakdown in swirling jets and wakes, have partly addressed this issue. In particular they have shown that highly rotational flows at large Reynolds numbers could exhibit various breakdown modes, referred to as bubble, helical

or double-helical. The influence of a jet-like and wake-like axial velocity profile was also investigated and revealed to promote the axisymmetric mode in the case of a jet-like vortex, or non-axisymmetric breakdown modes for wake-like vortex.

In light of these previous studies, a comprehensive analysis of a flow characterized by the concomitance of the previously cited effects - smooth boundary layer separation, vortex-wall and vortex-vortex interaction, strong upstream and upward external flow, strong adverse pressure gradient - such as the one presently investigated is, to the authors knowledge, only poorly, if not, documented.

As such this paper aims at providing a detailed description of the vortex structures that develop in the aft fuselage region and in the close wake of a simplified military transport aircraft. The analysis of the flow relies on two- and three-component Particle Image Velocimetry (PIV) measurements combined with a vortex-tracking approach. The present study is a step towards a more comprehensive knowledge of the complex physics driving such flows. It also constitutes a step towards the definition of future flow control strategies dedicated to the mitigation of the influence of the upsweep vortices on airdrop operations.

2 Experimental Approach

2.1 Wind Tunnel Model

The wind tunnel model, detailed in [20], is a simplified $1{:}16^{th}$ scale model of a Lockheed C-130 Hercules (figure 1) with a fuselage length-to-diameter ratio $L/D = 7$. The geometrical simplifications consist in the modification of the nose to a parabolic shape and the removal of both the vertical stabilizer and the main wing. The first two modifications (nose and stabilizer) do not alter the flow field in the region of interest (aft part of the fuselage and wake). Meanwhile they considerably reduce the manufacturing effort of this model and facilitate meshing process and computational efforts for Computational Fluid Dynamics (CFD) applications led in parallel to this study [4, 5, 21].

The presence of the main wing normally induces a downwash effect on the empennage and rear fuselage, particularly since flaps are partially down, as configured for an airdrop operation. In the aft fuselage portion, the relative flow is however partly counterbalanced by the few degrees positive angle of attack of the aircraft during airdrop. This downwash tends to mitigate the longitudinal pressure gradient that occurs in the cargo-bay ramp region. Without the main wing, the adverse pressure gradient is to be greater than it is actually [1]. In the present application, those two combined effects, downwash and positive angle of attack, were simulated by correcting the angle of attack of the simplified C-130 Hercules. It was thus determined to achieve PIV measurements at $0°$ angle of attack, as a reference test bench for airdrop considerations.

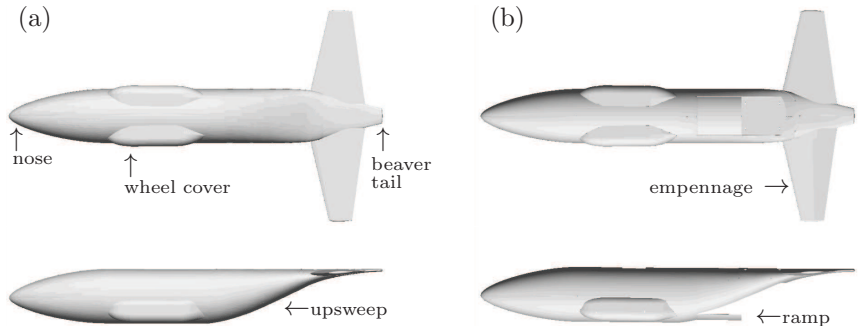

Fig. 1 Simplified C-130 geometry depicting lower view (top) and side view (bottom) of the closed (a) and opened (b) cargo-door and ramp configurations

Fig. 2 View of the wind tunnel model and of its strut arrangement (left) and detail of the downstream 2C-PIV camera (right)

2.2 Wind Tunnel Facility

The wind tunnel experiments were conducted in the ISAE/S4 subsonic wind tunnel facility. It is an Eiffel-type closed loop wind tunnel, with an opened 3m $\times$ 2m elliptical test section. The wind velocity U_∞ was fixed to 40m/s for a Mach number $M_\infty = 0.115$. The resulting fluctuating intensity in the working test section is below 0.4%. The model was positioned upside down, in the centre of the wind tunnel test section (figure 2). In this way, the two tandem masts linking the model to the weighting system had no influence on the upsweep region and its resulting wake. Considering the frontal area of the wind tunnel model relative to the surface of the test section, the wind tunnel blockage ratio was below 1.1%.

2.3 Reynolds Number Effect

For a free stream velocity U_∞ equal to 40m/s, at sea level ISA, the $1{:}16^{th}$ scale results in relatively small Reynolds number Re_L, close to 4.89×10^6 (based on fuselage length L). This Reynolds number is between 22 and 29 times smaller than the actual Reynolds number on a full scale C-130 Hercules,

depending on airdrop speed (typical airdrop speeds range from 110 to 140 Kts). Consequently, to force the boundary layer turbulent transition (for free stream velocities ranging from 20 to 40m/s), tripping strips were used on the nose, wheel covers and upper and lower surfaces of the empennage. Preliminary tests relying on the sublimation of a thin naphtalen layer applied on the skin of the model revealed that two consecutive, 10mm spaced, 280μm thick tripping strips are necessary to ensure a turbulent boundary layer on the whole body.

Despite this quite low Reynolds number, Epstein and coworkers [3], in their experimental investigation of the flow field about an upswept afterbody, observed no clear dependence on Reynolds number. Their analysis was based on static and total pressure contours in the wind tunnel model wake, pressure tap measurements on the upsweep base of the model, and five-hole probe crossflow velocity measurements in the model wake. The Reynolds number, based on fuselage length L, was varied from $Re_L = 0.58 \times 10^6$ to $Re_L = 1.66 \times 10^6$. The authors noticed that 'the vortex evolution appeared to be, at most, weakly related to Reynolds number'. They related it to the common modelization of most wake structures as incompressible and inviscid flows.

In the present work, in order to evaluate the Reynolds number effect in an experimentally accessible range, load measurements were achieved at four different free stream velocities $U_\infty = 20$, 30, 35 and 40m/s, resulting in Reynolds number from $Re_L = 2.44 \times 10^6$ to $Re_L = 4.89 \times 10^6$. Angle of attack was varied in the range $-5°$ to $+10°$. Different wind tunnel model configurations were tested, amongst which the closed and opened cargo-door and ramp configurations. These load measurements did not highlight any visible Reynolds number effect on the lift and drag *vs.* angle of attack evolution curves. This corroborates results and conclusions from [3].

However, it should be noted that the above-mentioned conclusions are limited to a narrow range of Reynolds numbers, which do not allow to extrapolate their validity to Reynolds numbers representative of flight conditions at full scale. In order to further investigate the Reynolds number effect in a wider Reynolds number range, complementary numerical computations were achieved following the approach described in [20]. The Reynolds number Re_L was thus varied by a factor of 16, from $Re_L = 0.61 \times 10^6$ to $Re_L = 9.78 \times 10^6$ (corresponding to the fifth of the actual Reynolds number on a full scale C-130 Hercules) and the incompressible, fully turbulent flow past the model at $0°$ angle of attack was determined by solving the Reynolds Averaged Navier Stokes equations with a $k - \omega$ SST Menter turbulence model. The analysis was based on both the evolution of the drag and lift coefficients of the wind tunnel model and the global flowfield topology, in terms of streamwise vorticity iso-contours in the aft part and in the close wake of the model, as a function of the Reynolds number. The lift coefficient, in very good accordance with the wind tunnel experiments at $Re_L = 4.89 \times 10^6$, was found to vary from less than 3.5% as Re_L was varied in the full range $[0.61 \times 10^6, 9.78 \times 10^6]$. The drag coefficient, overestimated by 8% in comparison with the wind tunnel experiments at $Re_L = 4.89 \times 10^6$, depicted an assymptotic decrease as Re_L was increased. As such, its variation was of the

order of 25% in the range $Re_L \in [0.61 \times 10^6, 2.44 \times 10^6]$, and lower than 17% in the range $Re_L \in [2.44 \times 10^6, 9.78 \times 10^6]$. Lastly, the global topology of the vorticity iso-contours was retained as Re_L was varied, and the position of the vorticity pockets, defined as closed lines of streamwise vorticity iso-contours and representative of the vortices that develop in the aft part and in the close wake of the model, was only moderately affected by the Reynolds number. In light of the above, the Reynolds number effect can thus be considered as non-critical for the following study.

2.4 PIV Measurements

Particle Image Velocimetry (PIV) cross-sectional measurements were led to precisely investigate the physics of the flow in the upsweep region and in the wake of the aircraft. They comprised three-component PIV measurements (3C-PIV) in the wake of the model and two-component PIV measurements (2C-PIV) in the upsweep region. The 3C-PIV technique was not applicable in this region because of masking effects induced by the model, and laser reflections on the ramp and upsweep walls.

The PIV system was a Hub-type Dantec Dynamics system. It was composed of a laser illumination source, two highly sensitive digital imaging devices, and dedicated hardware and software for laser/cameras synchronization, data acquisition and analysis. The illumination source was a frequency-doubled, double-cavity Nd:YAG laser operating at a wavelength of 532nm (200mJ/7ns per pulse) and a tuneable pulse rate up to 15Hz. The overlapped core beams were expanded into a 17° diverging light sheet using focusable sheet-forming optics. At the measurement station, the sheet thickness was adjusted to approximately 3mm. Recording of particles image pairs was accomplished *via* two 8-bit double-frame CCD cameras with a sensor resolution of 1600×1200 pixels^2. Those cameras were equipped with two Nikon 85mm f/1.8D lenses for 3C-PIV measurements. A Nikon 105mm f/2D lens was used for the 2C-PIV measurements.

The flow seeding, composed of water-based spherical particles, was produced by a fog generator equipped with a 2μm filter. The seeding granulometry was determined with a Dantec Phase Doppler Anemometry (PDA) system. It was found to be polydispersed in the range $0.4\mu\text{m} - 2\mu\text{m}$, with a mean particle diameter of 1.5μm. The seeding particles response time was estimated to 7μs [22]. Defining the cut-off frequency of the particle-flow system as the fluctuation frequency of the flow velocity for which the particle response, in amplitude, has decreased by 3dB, or 30%, the particles are therefore supposed to follow velocity fluctuations close to 23kHz. This can legitimately be considered as largely over most of the turbulence scales of interest in such wake investigations.

Two different PIV setups were developped for 2C- and 3C-PIV measurements respectively (figure 3). For the 2C-PIV cross-sectional measurements, the laser was positioned above the test section, out of the wind, on a three-

axial computer-driven displacement system. The precision of the laser sheet positioning along the centerline of the test section (x axis) was $\pm$0.5mm. The camera was fixed on an aerodynamically streamlined supporting frame, located 2.5m downstream the wind tunnel model, and facing a 40m/s wind (figure 2). This induced medium frequency (a few tens of Hz)/low amplitude (below $\pm$0.35mm) oscillations of the setup. A slight, low frequency (0.6Hz)/low amplitude ($\pm$1.5mm) oscillation of the model was also observed in the cross-sectional direction ((y, z) plane). Those oscillations were globally responsible for a $\pm$2mm positioning uncertainty between the camera and the model. It should be noted that this spatial inaccuracy, of the order of the PIV grid resolution, only acts as a static uncertainty between two consecutive, 100ms time-sampled, velocity vector maps. Each instantaneous vector map is actually resolved in a time scale (typically, a few tens of microseconds) orders-of-magnitude shorter than those vibrations time scales. In the present investigation, the optimal time interval between the two laser pulses used for the determination of a velocity vector map was equal to 40μs. This time scale is still assumed to be much lower than most of the turbulence time scales of interest here. For the 3C-PIV cross-sectional measurements, the laser positioning was kept as previously described. The two PIV cameras were positioned out of the wind, upstream the model. A pair of special mounts that allowed for the rotation of the camera body with respect to the lens was used, so as to meet the Scheimpflug condition. They were fixed on two mono-axial computer-driven displacement tables, aligned with the centerline of the test section. It resulted in camera positioning inaccuracy, along the x axis, below 0.1mm. Positioning uncertainty between the cameras and the model was thus only induced by the model oscillation. It was limited to $\pm$1.5 mm in the (y, z) plane.

Processing of the images to derive instantaneous velocity vector maps was done using an adaptive and deforming windowing cross-correlation technique combined with a high accuracy sub-pixel interpolation scheme [23,24]. Each image was divided into 32$\times$32 pixels^2 final interrogation areas, with 50% overlap. This yielded raw vector fields of up to 165$\times$160 vectors, for measurement plane dimensions of approximately 400 by 300 mm^2. It resulted in a measurement grid of spatial resolution ($\Delta x, \Delta y, \Delta z$) equal to 3$\times$2.8$\times$1.8 mm^3. The measurement grid spacing to fuselage diameter ratio was thus equal to 91 along y axis and 141 along z axis. This three-dimensional spatial resolution can be interpreted as the size of the elementary optical probe. It is expected to be small enough compared to most of the turbulence scales of interest in such wake flows. Finally, the global displacement r.m.s. error is assumed to be of the order of 0.1 pixel [25,26] (one should however keep in mind that this value is questionable and still challenging to accurately estimate in regions of strong spatial velocity gradients). For a 40μs time interval between cross-correlated images, the resulting uncertainty on instantaneous three-component velocity measurements is about 0.6m/s.

For each measurement plane, 300 pairs of image per camera were collected to evaluate the statistical characteristics of the flow. This number ensured the convergence of both first and second order statistics with a variance of less

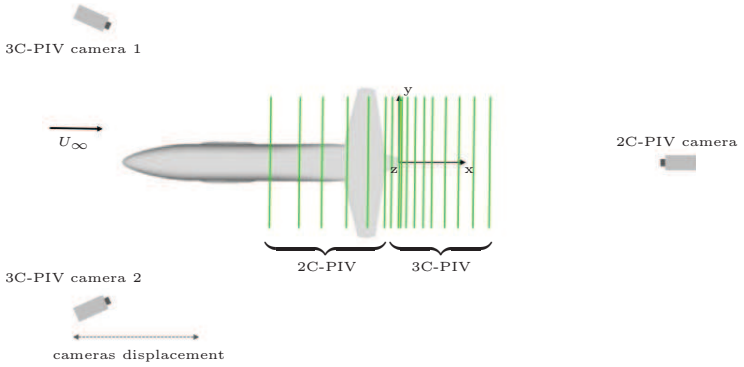

Fig. 3 Schematic view of the 2C- and 3C-PIV setups

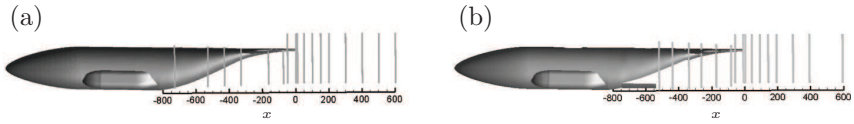

Fig. 4 Location of the 2C- and 3C-PIV cross-sectional measurement planes for (a) closed and (b) opened cargo-door and ramp configurations

than 5% at each point of the PIV measurement grid. Statistical calculations included mean velocities U_x, U_y, U_z and standard deviations σ_x, σ_y, σ_z along x, y and z directions, covariances and correlation coefficients. Because of the large amount of acquired data, in particular for 3C-PIV measurements, the number of scanned planes was limited to 16 for the closed cargo-door and ramp configuration and 17 for the opened cargo-door and ramp configuration. Those planes are depicted in figure 4. Note that for the closed configuration, 2C-PIV cross-planes located from x=-730mm up to x=-75mm were acquired during a prospective phase of the wind tunnel tests campaigns and restrict to the left hand-side of the flow. This was initially motivated by the need to predetermine the structure of the flow before a more comprehensive characterization, taking advantage of the (x, z) planar symmetry.

3 Vortex Tracking Method

On the basis of the mean velocity fields obtained from PIV, the vortex structures that develop in the aft portion and in the close wake of the fuselage are identified using the λ_2 criterion [27]. For each measurement plane, vortex cores are defined as connected regions Σ of negative λ_2. It is important to mention that λ_2 can be accurately computed on the basis of 2D flow fields since it has been verified that x-derivatives $\partial/\partial x$ of the velocity components are order of magnitude lower than the y- and z-derivatives $\partial/\partial y$ and $\partial/\partial z$. The vortex kinematic parameters are then determined as follows:

$$\Gamma = \iint_{\Sigma} \omega_x dydz \tag{1}$$

where ω_x refers to the longitudinal vorticity distribution in the core Σ and Γ is the vortex circulation.

The position (y_c, z_c) of the vortex centroid is then given by:

$$y_c = \frac{1}{\Gamma} \iint_{\Sigma} y\omega_x dydz \tag{2a}$$

$$z_c = \frac{1}{\Gamma} \iint_{\Sigma} z\omega_x dydz \tag{2b}$$

Three characteristic radii, denoted R_y, R_z and R respectively can be defined based on polar moments of vorticity [28]:

$$R_y = \left[\iint_{\Sigma} (y - y_c)^2 \omega_x dydz/\Gamma \right]^{\frac{1}{2}} \tag{3a}$$

$$R_z = \left[\iint_{\Sigma} (z - z_c)^2 \omega_x dydz/\Gamma \right]^{\frac{1}{2}} \tag{3b}$$

$$R = \left[\frac{1}{2}(R_y^2 + R_z^2) \right]^{\frac{1}{2}} \tag{3c}$$

The R_y/R_z aspect ratio gives an estimation of the vortex deformation in the (y, z) plane, revealing elliptical shape for instance.

As this project is concerned with airdrop problematics, it is interesting to examine the tangential and axial velocity components V_θ and V_x of the vortex core. Deployment of extraction or decelerating parachutes can actually be dramatically delayed due to aerodynamical efforts induced by these velocities. They are defined following equations 4a and 4b:

$$V_\theta = \frac{\Gamma}{2\pi R} \tag{4a}$$

$$V_x = \iint_{\Sigma} U_x dydz/\Sigma \tag{4b}$$

The vortex kinematics in the wake of the aircraft results in position, size and circulation variations. Besides, the decrease in vortex circulation, downstream the aircraft, which comes with an increase in vortex size, is partly influenced by the surrounding flow turbulence, and by velocity fluctuations within the vortex core. Its estimation is thus an essential parameter in such flow field investigation. On the basis of the mean velocity (U_x, U_y, U_z) and standard deviations (σ_x, σ_y, σ_z) flow fields, the fluctuating intensity i' of the vortex core is computed following equation 5:

$$i' = \iint_{\Sigma} \left[\sqrt{\frac{1}{3}(\sigma_x^2 + \sigma_y^2 + \sigma_z^2)} / \sqrt{(U_x^2 + U_y^2 + U_z^2)} \right] dydz/\Sigma \qquad (5)$$

As evoked in the introductive part of this document, the concomitance of smooth boundary layer separation, vortex-wall and vortex-vortex interactions, strong upstream and upward external flow and strong adverse pressure gradient are expected to promote several instabilities that are to affect the vortex core dynamics, amongst which meandering or vortex breakdown. Considering this study in an applicative light, and in particular in the context of airdrop operations, the response time of any airdropped object (payloads or paratroopers) is of the order of (or below) the Hertz. It is thus essentially sensitive to the mean flow and 'feels' any temporal variation of the flow at a given location in the close wake of the aircraft, whatever its origin - meander, vortex breakdown, boundary layer and wake turbulence -, as 'fluctuations'. As such and since this is of practical interest for the applicative concerns considered here, meandering, vortex breakdown and any other flow instability will be considered as contributive parts of the flow fluctuations and will be included in the terminology 'fluctuations', on an equal level with boundary layer and wake turbulence.

The determination of the kinematic parameters obtained for each vortex core finally allows the characterization of the vortical activity in the aft region and in the wake of the aircraft through their tracking from successive cross-sectional measurement planes.

4 Results

This section presents PIV results obtained for both the closed and the opened cargo-door and ramp configurations. First a global overview of the mean flow pattern is given, then a more detailed analysis of the vortical activity is proposed on the basis of the vortex tracking results.

4.1 Closed Cargo-Door and Ramp Configuration

The global description of the flow in the upsweep region and in the wake of the model is based on the x-vorticity and velocity fields depicted in figures 5 to 7. From the starting cross-section of the upsweep region up to the leading edge of the empennage, corresponding to longitudinal stations x=-730mm to x=-330mm, a vorticity pocket develops close to the left and right lateral walls of the fuselage (figure 5). A strong downward flow is observed in this area, while an upward flow is present in the central region close to the mid-plane of the aircraft (see figure 6). The convergence of those downward and upward flows, influenced by the longitudinal adverse pressure gradient occurring in the upsweep region, results in the separation of the fuselage boundary layer from the geometry and its longitudinal rolling up into the upsweep vortex. This

vortex then strongly interacts with the lower side of the empennage, as shown in figure 5 at x=-75mm. Its cross-section shape flattens in contact with the wall, leading to a typical elliptical shape.

This wall/vortex interaction causes the flow within the boundary layer of the empennage to separate. It induces a counter-rotating vortex, the 'induced' vortex. This vortex is initially pushed away from the plane of symmetry of the aircraft (figure 5, x=0mm to x=100mm). Downstream the model, on both sides of the mid-plane, those two counter-rotating vortices jointly move along helical trajectories. Concomitantly the vortices, and more particularly the induced one, shift towards the mid-plane, as their shapes slowly change from elliptical to circular (figure 5, x=100mm to x=600mm). This will be further discussed on the basis of the vortex tracking analysis. While advected downstream the model, the induced vortices seem to dissipate much faster than the upsweep vortices, as their vorticity levels drastically decrease.

In parallel, the lack of momentum caused by the aft fuselage and by the upsweep and induced vortices is well detected in the wake of the model, as illustrated in figure 7. One can indeed measure local longitudinal velocity deficit by up to 50% compared to the free stream velocity, just after the trailing edge of the empennage, in the core of the upsweep vortices. Finally the upwash effect caused by these vortices induces the aft fuselage wake to move upward while advected downstream the model (figure 7, close to the mid-plane).

Much more detailed information on the vortical activity is obtained from the vortex tracking approach. Figure 8 represents the 3D trajectories of the upsweep and induced vortices in the upsweep region (left-hand side of the geometry) and in the wake of the model (left and right-hand sides). For sake of clarity, only left-hand side vortex trajectories are depicted on the (x, z) view.

In particular, those data precisely reveal the position of the upsweep vortex core along the lateral wall of the aft fuselage portion, upstream the separation zone. The initial z-position of the vortex core, at cross-section x=-730mm, is about the third of the fuselage diameter. It is interesting to notice that it coincides with the mid-height position of the paratrooper door on the actual Lockheed C-130. The trajectory of the upsweep vortex core roughly follows the upsweep curvature. However its slope is slightly reduced by the local downward flow. When the upsweep vortex interacts with the empennage, its initially centre-directed core trajectory is deflected to the outside. Further downstream, the trajectories of the different vortex cores tend to align with the free stream direction.

The evolution along the x-direction of the parameters R, R_y/R_z, Γ, i', V_θ and V_x are illustrated in figure 9, for the upsweep and induced vortices. Taking advantage of the symmetry, only the vortices located on the left-hand side of the mid-plane will be analyzed. Besides, it has to be noticed that V_x and i' are only computed in the range $x \in [-50\text{mm}; 600\text{mm}]$ since they require the three components of the velocity flow fields (see equations 4b and 5).

Between cross-sections x=-730mm and x=-330mm, the upsweep vortex core starts to grow linearly (figure 9(a)). Its aspect ratio is initially quite low,

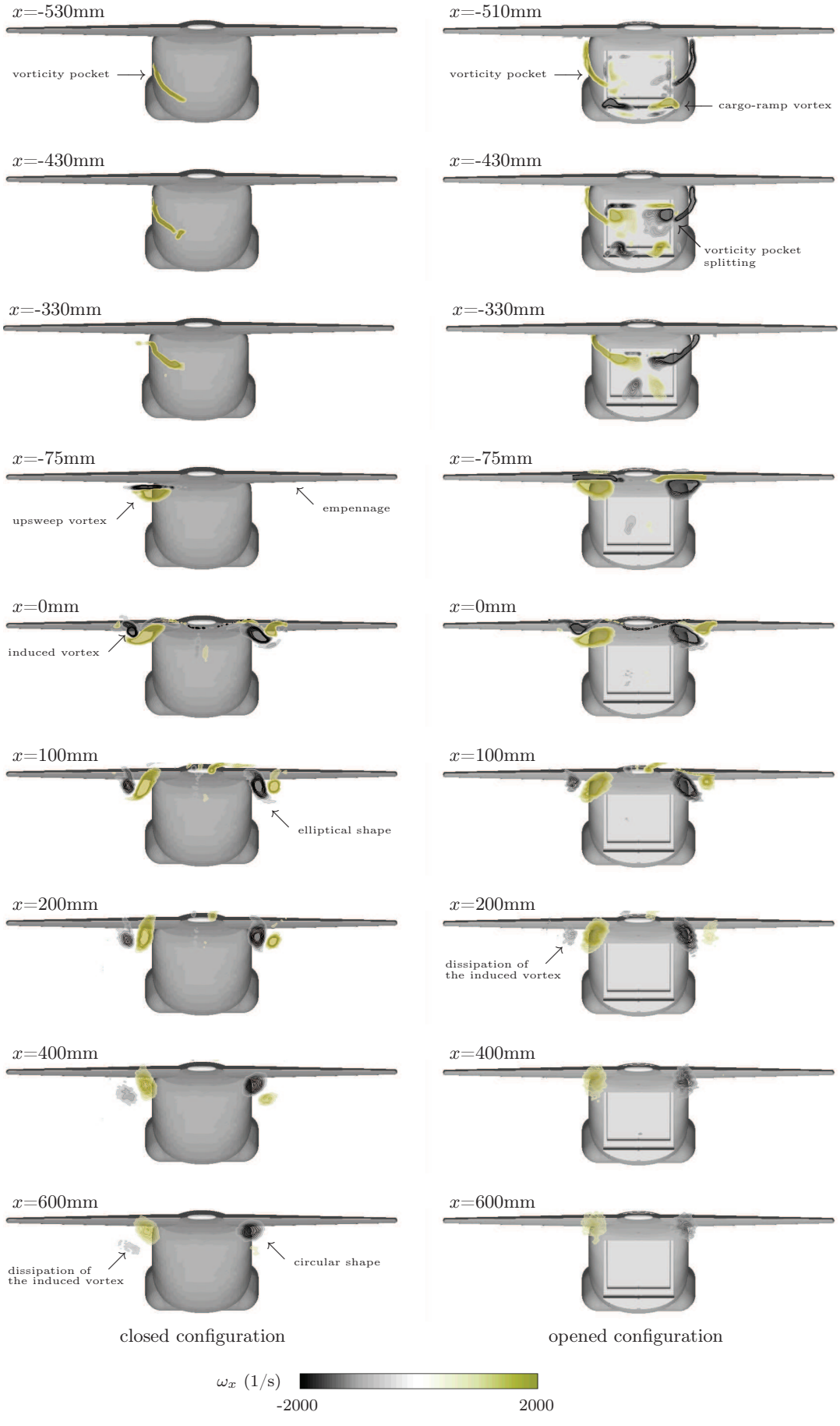

Fig. 5 ω_x vorticity isolines for closed and opened cargo-door and ramp configurations (ω_x faded-color isocontours are added for graphic rendering)

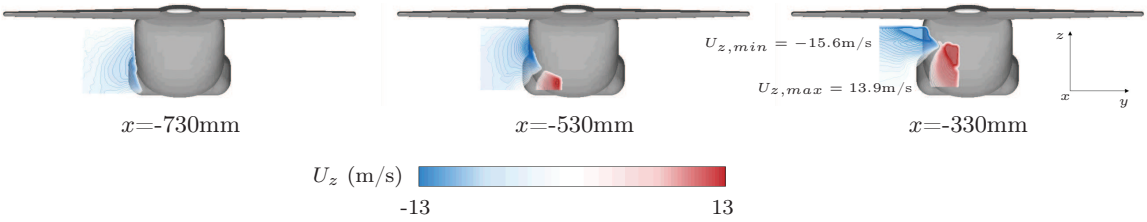

Fig. 6 U_z velocity isolines in the upsweep zone of the closed cargo-door and ramp configuration (U_z faded-color isocontours are added for graphic rendering)

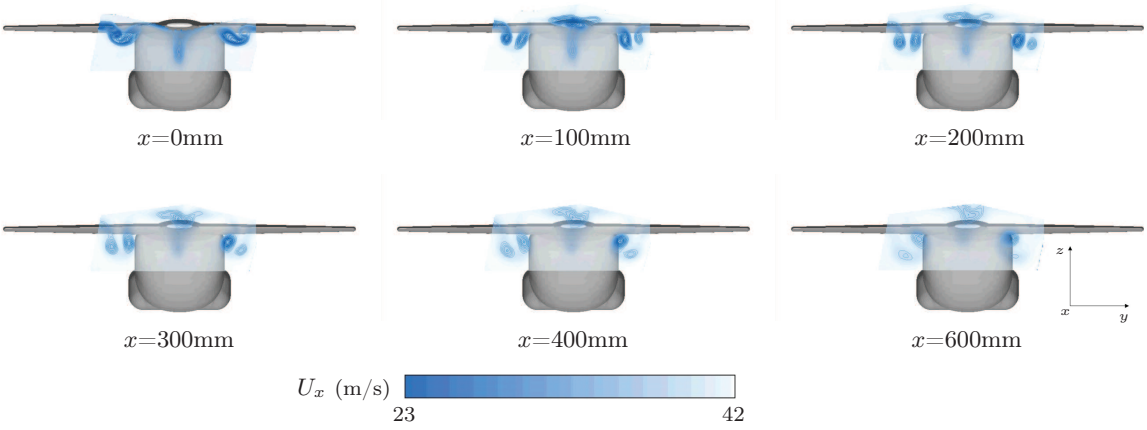

Fig. 7 U_x velocity isolines in the near wake of the closed cargo-door and ramp configuration

close to 0.5, as the vorticity pocket is initially stretched in the z-direction, along the aft fuselage. As the vortex moves along the upsweep part of the aft fuselage, separates from the geometry while approaching the leading edge of the empennage around x=-330mm, and interacts with the lower surface of the empennage up to x=-75mm, its aspect ratio rapidly increases up to 2.27 (figure 9(b)). This is due to, first, the shifting of the vorticity pocket along the evolving cross-sections of the aft fuselage (see figure 5), inducing its geometrical rotation around the x-axis, and second to the vortex/empennage interaction, accentuated by the strong upward flow in this area that tends to push the vortex against the wall of the empennage. As previously mentioned, the upsweep vortex flattens on the lower side of the empennage. This also induces a strong decrease of its mean radius, close to section x=-165mm.

The vortex/empennage interaction generates the induced vortex. Its initial shape is also elliptical and its main axis is aligned with the y-axis, explaining its high aspect ratio, grossly equal to the aspect ratio of the upsweep vortex in this area. Just after its 'rebound' on the empennage, between x=-165mm and x=-75mm, the elliptically-shaped upsweep vortex starts to rotate around its axis, explaining its decrease in aspect ratio.

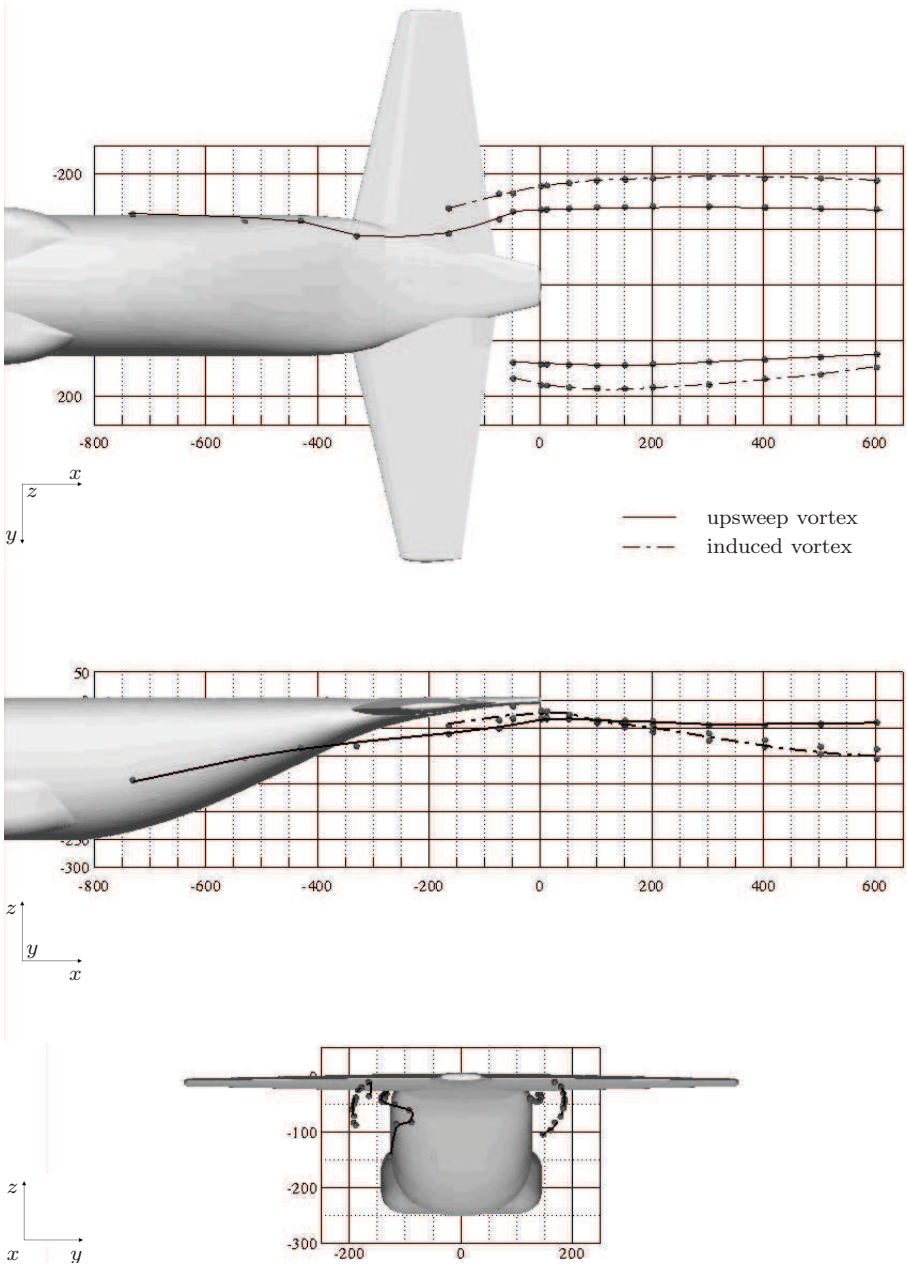

Fig. 8 3D trajectories of the upsweep and induced vortices for the closed cargo-door and ramp configuration

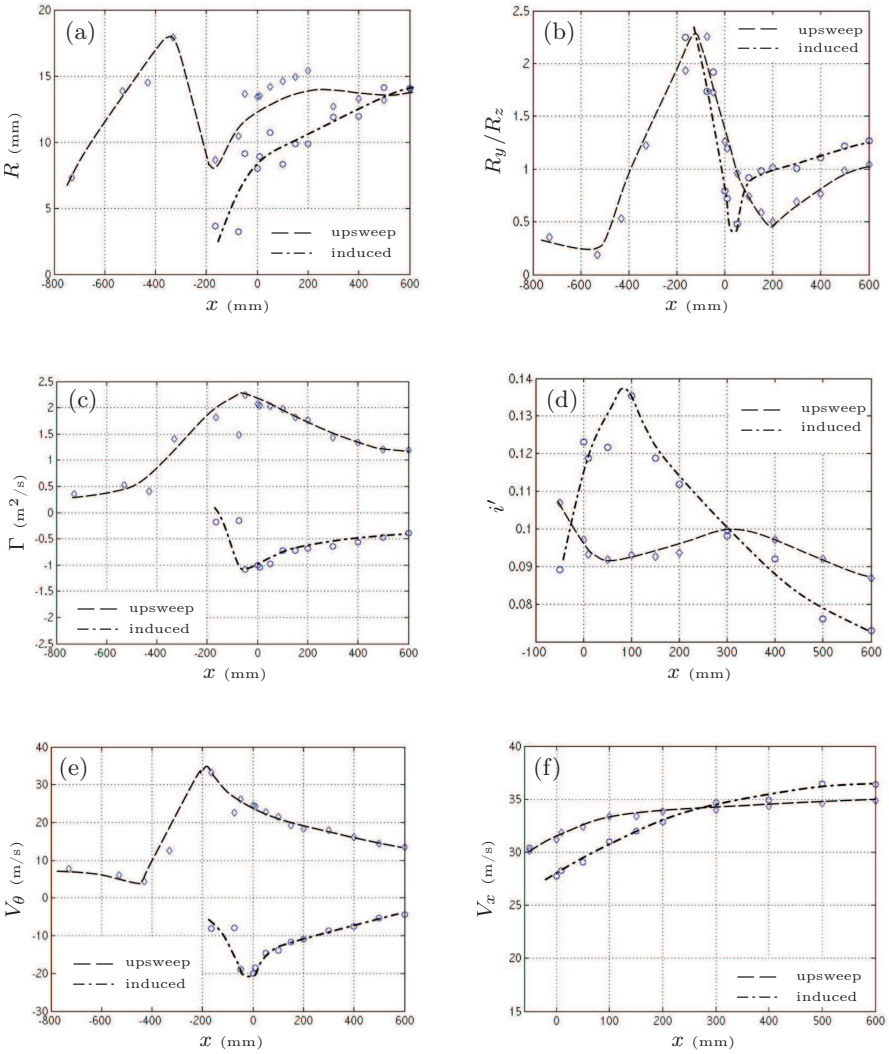

Fig. 9 longitudinal evolution of the (a) core radius R, (b) radii aspect ratio R_y/R_z, (c) circulation Γ, (d) fluctuating intensity i', (e) tangential velocity V_θ and (f) axial velocity V_x of the left hand-side upsweep and induced vortices, for the closed cargo-door and ramp configuration

As the vortex moves downstream, the trajectory of the upsweep vortex is no more subjected to the strong upwash flow, imposed by the upsweep zone, that maintained it close to the wall. Its radius is now free to expand. After x=-75mm, the upsweep and induced vortices are jointly advected in the wake of the model. Due to turbulent diffusion, their radii progressively increase. As they move along helical trajectories (figure 8), the resulting rotation still

induces a decrease of the aspect ratio R_y/R_z around 0.5, until they tend to get circular because of turbulent diffusion effects.

Figure 9(c) depicts the longitudinal evolution of the circulation Γ of the upsweep and induced vortex cores. From x=-730mm to x=-75mm, due to the proximity of the walls (aft fuselage wall from x=-730mm to x=-330mm, lower side of the empennage from x=-255mm to x=-75mm) both upsweep and induced vortex cores are vorticity-fed by the boundary layer, resulting in an increase of their circulation. $|\Gamma|$ is thus maximum immediately after the trailing edge of the empennage, at cross-section x=-50mm. The upsweep vortex circulation is then 2.25 times higher than the induced vortex circulation. Downstream the model, those vortices diffuse due to the shear imposed by the outer flow, inner turbulence (coming from the boundary layer separations) and, to a lesser extent, viscous effects, and their respective circulations decrease by 47% for the upsweep vortex and by 64% for the induced vortex, at x=600mm.

Figure 9(d) displays quite high fluctuating intensities i' within the vortex cores. Such high levels partly arise from the very history of the upsweep and induced vortices which result from the separation and the rolling-up of the fuselage and empennage boundary layers respectively, and from meandering and transient vortex breakdown events. Yet one can observe that the fluctuating intensity in the core of the upsweep vortex ($\sim$ 11% at x=-50mm) is greater than that of the induced vortex ($\sim$ 9%), highlighting 1) a more or less developed state of the boundary layers before their separation, 2) a longer transit time of the upsweep vortex in the upsweep zone, causing a larger influence of both vortex/wall interaction in the meandering process and of the adverse pressure gradient in the vortex breakdown process. Subsequently the induced vortex experiences a drastic increase of its fluctuating intensity up to 14% at $x \approx$ 100mm, under the influence of complex unsteady upsweep/induced vortex interactions. Conversely the upsweep vortex is less affected by these interactions and exhibits weaker variations of i', between 9 and 10%. Eventually these high levels can explain the decay of the vortex circulations along the x-axis.

Figures 9(e) and (f) illustrate the evolution of the tangential and axial velocities V_θ and V_x of the upsweep and induced vortex cores. The tangential velocity of the upsweep vortex is initially low in the aft fuselage portion, but it drastically increases as the vortex separates from the fuselage and interacts with the empennage. The maximum velocity is reached at cross-section x=-165mm, through the angular momentum conservation, when the upsweep vortex flattens against the empennage and experiences a sharp decrease of its radius under the influence of a strong upward flow. It is then equal to 34m/s. As it generates the induced vortex, its tangential velocity starts to decrease, while the tangential velocity of the induced vortex begins to increase, reaching a maximum value of -20m/s at cross-section x=0mm. The tangential velocity of the two vortices then decreases, by 61% for the upsweep vortex and by more than 80% for the induced vortex, at cross-section x=600mm. The axial velocity of the upsweep and induced vortex cores, only measured from cross-section x=-50mm to x=600mm, progressively increases as the vortices diffuse and are accelerated by the outer flow.

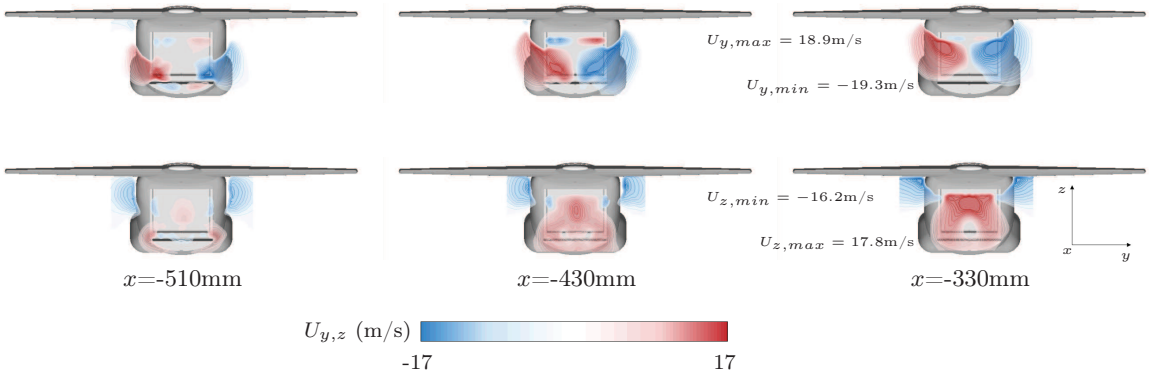

Fig. 10 U_y (upper line) and U_z (lower line) velocity isolines in the upsweep zone of the opened cargo-door and ramp configuration (U_y and U_z faded-color isocontours are added for graphic rendering)

4.2 Opened Cargo-Door and Ramp Configuration

This last section presents results for the opened cargo-door and ramp configuration. Because of masking effects induced by the cargo-ramp, it was not possible to achieve measurements upstream the end of the ramp. The first PIV cross-section plane thus starts at x=-510mm. As shown in figures 5, 10 and 11, the opened cargo-bay cavity complexifies the flow field topology and the vortex dynamics at the rear of the fuselage and in the wake of the model. The vorticity pocket that initially develops near the lateral-side wall of the aft fuselage, on both sides of the aircraft, splits in two separate structures when it reaches the edge of the cavity (see figure 5, x=-430mm). In this area, which corresponds to the payloads extraction area, a strong incoming flow is observed (figure 10, upper line), oriented towards the mid-plane of the geometry. In the central region, a significant upward flow occurs (figure 10, lower line). Ascendant U_z velocities of the order of 17.8m/s are measured at cross-section x=-330mm. This upward flow is stronger than that observed for the closed configuration, where the maximum U_z velocity measured at x=-330mm is 13.9m/s.

The vortices resulting from the split of the initial vorticity pocket within the cargo-bay cavity then merge around cross-section x=-255mm (figure 12), under the influence of the empennage proximity. The resulting upsweep vortex is then advected downstream the aircraft, following a quasi rectilinear and very faintly ascending trajectory, contrary to the closed configuration, where the upsweep vortex exhibits a typical helical trajectory. The trajectory of the induced vortex also slightly differs from that of the closed configuration. Figure 12 clearly depicts those trajectory modifications. As the twisting movement of the upsweep and induced vortices is less pronounced in the present configuration, the induced vortex, initially pushed away from the plane of symmetry of the aircraft, continues to deviate away from the mid-plane. After cross-section x=400mm this vortex is no more detected.

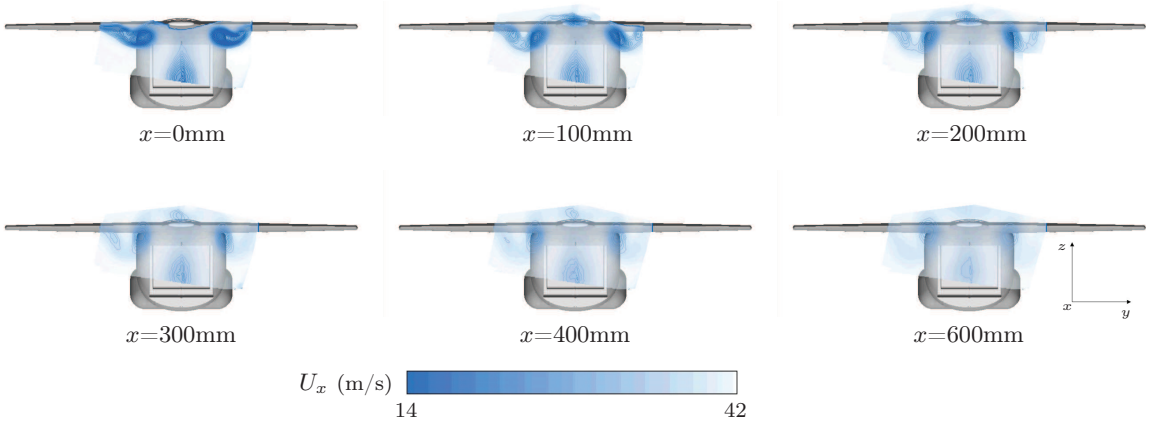

Fig. 11 U_x velocity isolines in the near wake of the opened cargo-door and ramp configuration

The strong upward flow observed in the central region aft of the cargo-bay (figure 10) generates two new pairs of counter-rotating vortices (figures 5 and 12), induced by the flow bypassing the cargo-ramp and the beaver-tail respectively. Because of the upwash effect, these vortices move upward as they are advected downstream the aircraft. Concomitantly their intensity rapidly decays, as revealed by the evolution of their vorticity levels. The cargo-ramp vortices also tend to shift towards the mid-plane of the geometry, under the influence of the incoming flow that occurs in this region, and lose their spatial coherence. Indeed, beyond cross-section x=-50mm, they are interpreted as multiple smaller vortex cores by the vortex tracking method. The features of those cargo-ramp and beaver-tail vortices, if interesting to notice for purposes of CFD computations validation, will not be analyzed in more detail since they do not interfere with airdrop issues.

The lack of momentum caused by the aft fuselage and by the upsweep and induced vortices is clearly visible in the wake of the model, as illustrated in figure 11. One can indeed measure local U_x velocity deficit in the core of the upsweep vortices by up to 62% compared to the free stream velocity, just after the trailing edge of the empennage. Moreover, the opened cargo-bay cavity imposes a larger velocity deficit region than the closed configuration.

The evolution in the x-direction of the vortex core parameters R, R_y/R_z, Γ, i', V_θ and V_x also reveals noticeable differences compared to the closed configuration. They are depicted in figure 13.

At cross-section x=-330mm, in the extraction area, three distinct vortex cores are identified. These vortex cores originate from two consecutive splits of the upsweep vorticity pocket. The first split, denoted split#1, occurs as the vorticity pocket interacts with the cargo-bay cavity, as previously mentioned. Between x=-510mm and x=-330mm the two resulting vortex cores are quite similar in intensity and size and evolve along the upsweep region of the fuselage

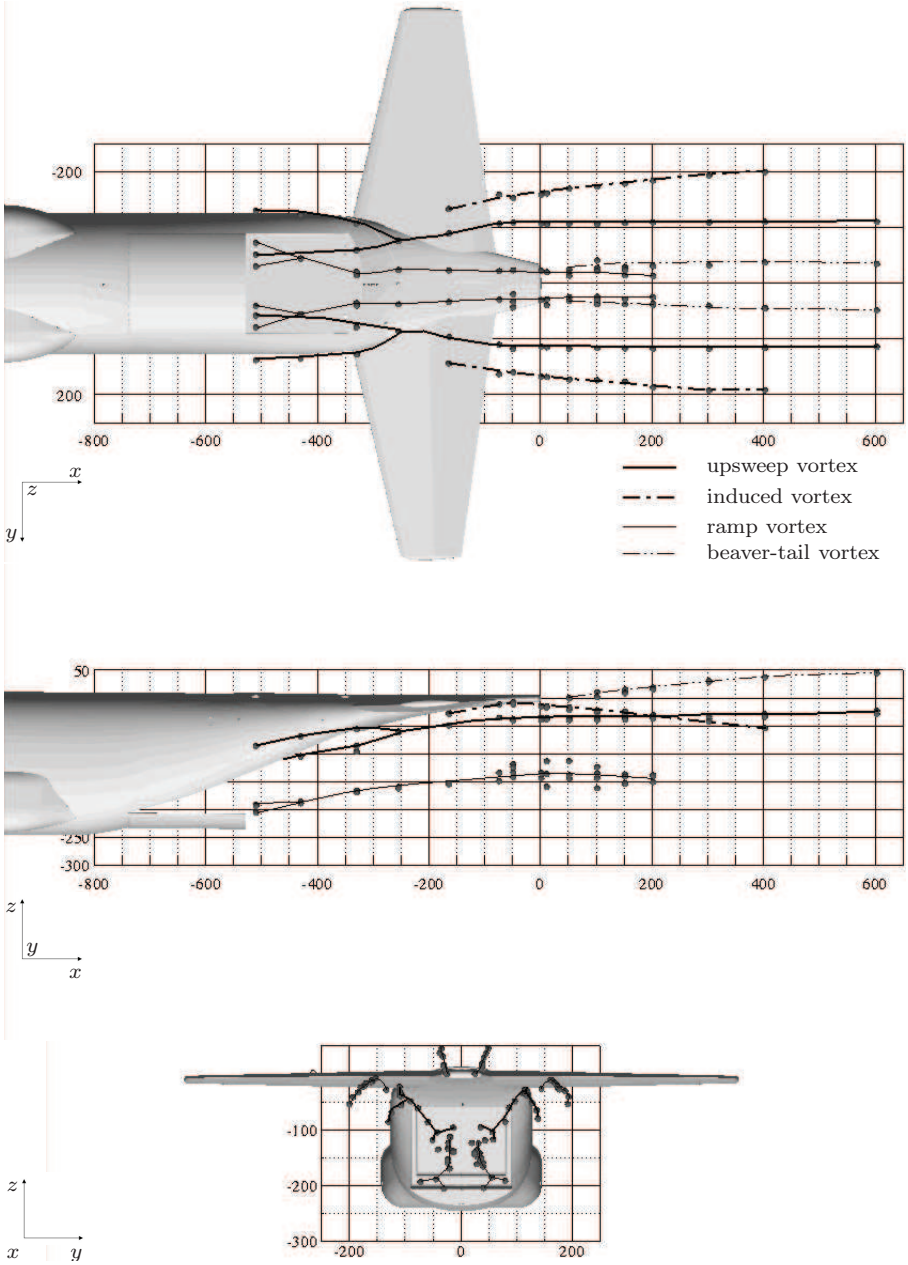

Fig. 12 3D trajectories of the upsweep, induced, ramp and beaver-tail vortices for the opened cargo-door and ramp configuration

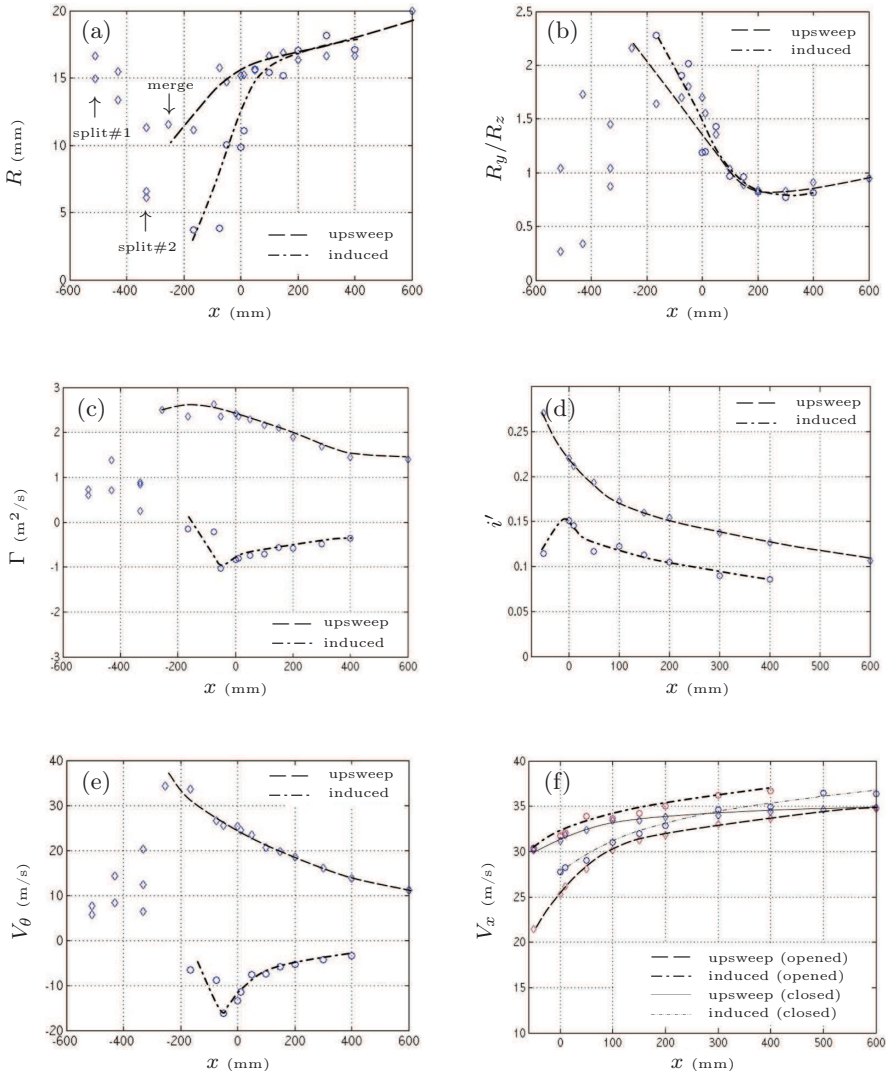

Fig. 13 longitudinal evolution of the (a) core radius R, (b) radii aspect ratio R_y/R_z, (c) circulation Γ, (d) fluctuating intensity i', (e) tangential velocity V_θ and (f) axial velocity V_x of the left hand-side upsweep and induced vortices, for the opened cargo-door and ramp configuration

and inside the cargo-bay cavity respectively. The latter undergoes a second split, denoted split#2, close to section x=-330mm (figures 13(a), (b), (c) and (e) and lower view of figure 12), leading to a third vortex core only visible on the rear view of figure 12 (since it is in conjunction with other cores in the (y, z) view and masked by the geometry in the (x, z) view). Once again it is interesting to notice that the vortex cores resulting from split#2 exhibit

similar radius R, aspect ratio R_y/R_z, circulation Γ and tangential velocity V_θ. Eventually the three vortex cores merge around cross-section x=-255mm (figure 12) into the upsweep vortex.

Since the comparison between the closed and opened cargo-door and ramp configurations requires to be based on analogous vortical entities, it will only be achieved from cross-section x=-255mm, *i.e.* after the vortex merging. Similarly to the closed configuration, both the upsweep and induced vortex radii progressively increase when moving downstream the model. However, the vortex cores get larger in the opened configuration, by up to 30%, beyond cross-section x=200mm. Their aspect ratio tends to unity (reflecting their circular-shape recovery) following a monotonic trend, since their twisting motion downstream the aircraft is less pronounced than for the closed configuration. The intensity of the induced vortex is quite similar to that of the closed configuration, highlighting their similar formation process (separation and rolling-up of the empennage boundary layer). Nonetheless the induced vortex has greater axial and slightly lower tangential velocities (figure 13(e) and (f)). The evolution of the V_θ velocity of the upsweep vortex shows similar trend to that of the closed configuration. Its axial velocity V_x, initially lower than that of the closed configuration due to its partial transit inside the cavity, recovers quite similar values around x=300mm.

Finally, the most noticeable difference between the vortex features of the closed and opened configurations is the fluctuating intensity within the upsweep vortex core. It is much higher in the opened configuration, probably due to the successive splits and merging of the vortex, responsible for unsteady oscillations of the vortex. This may reveal transient instabilities responsible for higher velocity fluctuations. It is also possible to interpret this, at least upstream cross-section x=100mm, as a partial consequence of the local transit of the vortex inside the cargo-bay cavity, characterized by lower velocities. This vortex initially develops in the fuselage boundary layer. It implies that it gets initially high velocity fluctuation levels. Consequently this leads to higher fluctuating intensity when the vortex slows down inside the cavity, as the velocity fluctuation values may maintain. Such fluctuation levels, associated with stronger upward and incoming flow in the extraction area are typical concerns for airdrop problematics.

5 Conclusion

In this paper we have experimentally investigated the vortical activity in the close wake of a 1:16th scale simplified military transport aircraft. On the basis of wind tunnel 2C- and 3C-PIV measurements, a vortex tracking approach has been applied for two representative configurations of airdrop operations: the closed and opened cargo-door and ramp configurations.

The analysis brought to light a complex vortex dynamics, strongly influenced by flow/wall and vortex/vortex interactions, in the aft portion and in the wake of the aircraft. The closed configuration is characterized by the sep-

aration and the longitudinal rolling-up of the fuselage boundary layer into two counter-rotating upsweep vortices distributed on both sides of the aircraft plane of symmetry. The trajectory of these vortices is found to initiate close to the lateral paratrooper doors. Subsequently the vortices interact with the empennage and cause the separation of the empennage boundary layer, inducing a second pair of counter-rotating vortices. Both induced and upsweep vortices are then jointly advected downstream the aircraft following helical trajectories, while progressively dissipating. The opened configuration strongly differs in the increased complexity of the vortex core network that develops in the wake of the aircraft. As such it is shown that the upsweep vortices first undergo successive splits inside the cargo-bay cavity before merging in the vicinity of the empennage, promoting higher fluctuating intensity levels. The subsequent interaction of the upsweep vortices with the empennage boundary layer is similar to that observed for the closed configuration. However the consecutive upsweep and induced vortex trajectories are affected by a stronger upwash that tends to mitigate the helical motion in favour of ascending trajectories. This upwash is also responsible for the occurrence of two new pairs of counter-rotating vortices that originate from the cargo-ramp and the beaver-tail respectively.

Those phenomena -strong upwash in the cargo-bay region and velocity deficit in the wake, high fluctuating intensity levels in the vortex cores and in the wake of the aircraft, complex vortex network- constitute critical issues for airdrop operations. The exhaustive characterization proposed in this paper brings a new light on incidents encountered during operational missions. Furthermore it serves the definition of optimized procedures and of future flow control strategies in order to enhance airdrop safety, precision and efficiency.

Acknowledgements The authors gratefully acknowledge the French Ministry of Defence and the DGA for supporting this work. They are also thankful to the S4 wind tunnel staff for their technical support and to Richard Charles (US Army/Natick Soldier Research, Development and Engineering Center), Scott A. Morton (US Air Force/Eglin AFB), Keith Bergeron (USAFA/DFAN), Mick Vallence (RAF/JATEU) and Manfred Seeger (IABG, chairman of the AIA project) for their collaborative effort within the AIA project.

References

1. Wortman A, Reduction of fuselage form drag by vortex flows, J Aircraft, 36-3, 501-506 (1999)
2. Johnson W, Trickey C, Forsythe J, Albertson J, Leigh E, Experimental and computational investigation of the flow behind a C-130 with tailgate down, in 40^{th} AIAA Aerospace Sciences Meeting, Reno, Nevada, 14-17 January 2002 (2002)
3. Epstein R.J, Carbonaro M.C, Caudron F, Experimental investigation of the flowfield about an upswept afterbody, J Aircraft, 31-6, 1281-1290 (1994)
4. Morton S.A, Vignes B, Bury Y, Experimental and computational results of a simplified C-130 shape depicting airflow influence on airdrop, NATO RTO, AVT-133, Vilnius, Lithuania, 2-5 October 2006 (2006)
5. Bergeron K, Cassez J.F, Bury Y, Computational investigation of the upsweep flow field for a simplified C-130 shape, in 47^{th} AIAA Aerospace Sciences Meeting, Orlando, Florida, 5-8 January 2009 (2009)

6. Seeger M, Müller L, Carlsson P.K, Bury Y, de Lassat de Pressigny Y, Lallemand G, Vallence M, Wheeler R, Benney R, Charles R, Morton S.A, Tavan S, Four-Powers Long Term Technology Projects: Airflow Influence on Airdrop and 2^{nd} Precision Airdrop Improvements, in 18^{th} AIAA Aerodynamics Decelerator Systems Technology Conference and Seminar, Munich, Germany, 23-26 May 2005 (2005)
7. Shizawa T, Eaton J.K, Turbulence measurements for a longitudinal vortex interacting with a three-dimensional turbulent boundary layer, AIAA J, 30, 49-55 (1992)
8. Liu J, Piomelli U, Spalart P.R, Interaction between a spatially growing turbulent boundary layer and embedded streamwise vortices, J Fluid Mech, 326, 151-179 (1996)
9. Cottin C, Leweke T, Experiments on vortex pair dynamics in ground effect, in 6^{th} EUROMECH Fluid mechanics Conference, Stockholm, Sweden, 26-30 June 2006 (2006)
10. Duponcheel M, Cottin C, Daeninck G, Leweke T, Winckelmans G, Experimental and numerical study of counter-rotating vortex pair dynamics in ground effect, in 18^{th} Congrès Francais de Mécanique, Grenoble, France, 27-31 August 2007 (2007)
11. Roy C, Schaeffer N, Le Dizès S, Thompson M, Stability of a pair of co-rotating vortices with axial flow, Phys Fluids, 20, 094101 (2008)
12. González L.M, Gómez-Blanco R, Theofilis V, Eigenmodes of a counter-rotating vortex dipole, AIAA J, 46(11), 2796-2805 (2008)
13. Donnadieu C, Ortiz S, Chomaz J-M, Billant P, Three-dimensional instabilities and transient growth of a counter-rotating vortex pair, Phys Fluids, 21, 094102 (2009)
14. Ryan K, Butler C.J, Sheard G.J, Stability characteristics of a counter-rotating unequal-strength Batchelor vortex pair, J Fluid Mech, 696, 374-401 (2012)
15. Benjamin T, Theory of the vortex breakdown phenomenon, J Fluid Mech, 14, 593-629 (1962)
16. Sarpkaya T, Effect of the adverse pressure gradient on vortex breakdown, AIAA J, 12, 602-607 (1974)
17. Leibovich S, The structure of vortex breakdown, Annu Rev Fluid Mech, 10, 221-246 (1978)
18. Sarpkaya T, Vortex breakdown and turbulence, in 33^{rd} AIAA Aerospace Sciences Meeting and Exhibit, Reno, Nevada, 9-12 January 1995 (1995)
19. Ruith M.R, Chen P, Meiburg E, Maxworthy T, Three-dimensional vortex breakdown in swirling jets and wakes: direct numerical simulation, J Fluid Mech, 486, 331-378 (2003)
20. Bury Y, Bergeron K, Seeger M, Tricarico G, AIA - Airflow Influence on Airdrop - final report, 4Power Long Term Technology Project, Tech. Report, NATO (2009)
21. Claus M.P, Morton S.A, Cummings R.M, Bury Y, DES turbulence modelling on the C-130: comparison between computational and experimental results, in 43^{rd} AIAA Aerospace Sciences Meeting and Exhibit, Reno, Nevada, 10-13 January 2005 (2005)
22. Melling A, Tracer particles and seeding for Particle Image Velocimetry, Meas Sci Technol, 8, 1406-1416 (1997)
23. Lecordier B, Trinité M, Advanced PIV algorithms with image distortion - Validation and comparison from synthetic images of turbulent flow, in 5^{th} International Symposium on Particle Image Velocimetry, Busan, Korea, 22-24 September 2003 (2003)
24. Westergaard C.H, Madsen B.B, Marassi M, Tomasini E.P, Accuracy of PIV signals in theory and practice, in 5^{th} International Symposium on Particle Image Velocimetry, Busan, Korea, 22-24 September 2003 (2003)
25. Nobach H, Damaschke N, Tropea C, High-precision sub-pixel interpolation in particle image velocimetry image processing, Exp. in Fluids, 39, 299-304 (2005)
26. Raffel M, Willert C, Wereley S, Kompenhans J, Particle Image Velocimetry: a practical guide, 2^{nd} edition, Springer-Verlag, Berlin (2007)
27. Jeong J, Hussain F, On the identification of a vortex, J Fluid Mech, 285, 69-94 (1995)
28. Ting L, Klein R, Viscous vortical flows, Lecture Notes in Physics, Springer-Verlag, Berlin (1991)